Optical Fiber Technology 94 (2025) 104295

Contents lists available at ScienceDirect

Optical Fiber Technology

journal homepage: www.elsevier.com/locate/yofte

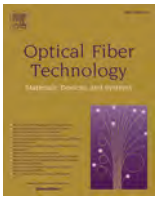

High-sensitivity strain sensor with air microbubble based on the Vernier effect

Jingwei Lv [a], Weijie Kong [a], Jianxin Wang [a], Wei Li [a], Renfeng Li [a], Liangliang Li [a], Qiang Liu [a], Jianing Shi [a], Wei Liu [a], Pan Meng [a], Xinrui Guo [a], Paul K. Chu [b], Chao Liu [a,*]

[a] School of Physics and Electronic Engineering, Northeast Petroleum University, Daqing 163318, PR China
[b] Department of Physics, Department of Materials Science and Engineering, and Department of Biomedical Engineering, City University of Hong Kong, Tat Chee Avenue, Kowloon, Hong Kong, China

ARTICLE INFO

Keywords:
Fabry-Pérot interferometer
Optical fiber sensor
Temperature cross-sensitivity
Strain
Vernier effect

ABSTRACT

A highly sensitive optical fiber strain sensor with simple structure, easy preparation and temperature insensitivity is proposed. It consists of a parallel Fabry-Pérot Interferometer (FPI) based on the Vernier Effect (VE). The sensing cavity (FPI_S) is formed by two single-mode fibers (SMFs) by fusion splicer arc discharge, and the reference cavity (FPI_R) consists of two SMFs inserted into a hollow capillary tube (HCT) . The sensor has a high strain sensitivity of −42.04 pm/με and an ultra-low temperature cross-sensitivity of 0.022 με/°C, which reduces the measurement errors caused by temperature variations. At the same time, stable experimental measurements show that the interference fringes change by less than 20 pm. This sensor combines high strain sensitivity, ultra-low temperature cross-sensitivity, and stable performance for precise strain measurement applications.

1. Introduction

High-sensitivity strain sensing technology, which employs advanced sensors for materials and structure evaluation, plays a very important role in medical monitoring and diagnosis, civil engineering, aerospace, structural engineering, automotive industry, and military fields [1–3]. Compared to conventional electrical sensors, optical fiber strain sensors have unique merits such as small size, remote monitoring capability, high flexibility, low propagation loss, low manufacturing cost, and resistance to electromagnetic interference [4–7]. Among them, optical fiber strain sensors based on the FPI has drawn significant attention because of its compact structure and easy fabrication. To obtain stable spectra and achieve high sensitivity, the cavity length and effective index of the cavity can be modulated by chemical etching [8,9], splicing technique [10,11] and femtosecond laser micromachining [12]. Despite considerable efforts, it is still difficult to produce shorter bubble length or thinner bubble wall, as the cavity lengths and walls have reached their limits [13]. Recent applications are demanding and better performance such as higher precision in strain measurements, and consequently, breakthroughs such as significant sensitivity improvement are necessary.

The VE is an effective method to augment the sensitivity of optical fiber strain sensors based on FPI. [14–18]. The VE, which is produced by taking two slightly detuned interference signals and overlapping them to form a vernier envelope, has better sensitivity than individual interferometers in the structure [19,20], and several strain sensors based on the VE have been proposed [21,22]. For example, Deng et al. have fabricated a strain sensor consisting of two cascaded FPIs using femtosecond laser pulse irradiation, with a strain sensitivity of 28.11 pm/με and a temperature sensitivity of 278.48 pm/°C [23]. Zhang et al. have utilized femtosecond laser micromachining to produce a strain sensor consisting of two parallel-connected FPIs with a strain sensitivity of −14.9 pm/με and a temperature sensitivity of 0 pm/°C [24]. Nevertheless, the manufacturing process requires expensive equipment and complex pre-processing, thereby increasing the cost and production complexity. Nan et al. have prepared a strain sensor consisting of open-cavity FPI and closed-cavity FPI in parallel showing a strain sensitivity of −43.2 pm/με and a temperature sensitivity of −27 pm/°C [13]. Zhang et al. have designed a strain sensor based on a cascaded Fabry-Pérot cavity and an optical fiber Sagnac loop exhibiting a strain sensitivity of 28.9 pm/με and a temperature sensitivity of 401.1 pm/°C [2]. Although expensive equipment and complex pre-processing can be avoided, there is a need to reduce measurement errors arising from temperature variations in order to further improve the strain sensitivity and to reduce the

* Corresponding author.
E-mail address: msm-liu@126.com (C. Liu).

https://doi.org/10.1016/j.yofte.2025.104295
Received 27 February 2025; Received in revised form 24 April 2025; Accepted 1 June 2025

temperature cross-sensitivity.

Herein, a parallel-structured fiber optic FPIs is designed based on the VE. The innovation lies in the simple process to realize high sensitivity sensing and effective suppression of temperature interference. The FPI_S is prepared by fusion splicer arc discharge of two SMFs to produce air microbubble, and The FPI_R is assembled with SMFs using HCT. The experimental results reveal that the parallel-structured fiber optic sensor has a high strain sensitivity of −42.04 pm/με, which represents 4.76 folds increase in the strain sensitivity compared to the single FPI_S. In the temperature range of 30-150°C, the temperature sensitivity and cross-temperature sensitivity of the sensor are 0.936 pm/°C and 0.022 με/°C, enabling efficient suppression of temperature disturbances. In addition, the sensor's excellent stability and repeatability offer significant potential for microdisplacement sensing applications.

2. Sensor fabrication and working principles

The fabrication process of FPI_S and FPI_R is simple and safe. The fabrication process of FPI_S is shown in Fig. 1(a). Firstly, the coated SMF was stripped, wiped with alcohol, then cut by a fiber cutter and the fiber was placed in an optical fiber fusion splicer (Fujikura 80 s). The SMF was moved close to the discharge electrode by driving motors. The discharging time was 1,000 ms and the power parameter was "-5". Multiple discharges were initiated to round and smooth the flat fiber ends. Then, the two SMF surfaces were immersed in a small amount of refractive index matching liquid, and then the SMF with both tips covered by the liquid were put back to the fusion splicer. The refractive index matching solution was an oil-based substance with good stability, fluidity and lower surface tension. Subsequently, by adjusting the driving motors on the fusion splicer and moving and aligning the cores of the two optical fibers in the X and Y planes, the two optical fibers were slightly squeezed, representing the state of being prepared and to be processed. The discharging time was 1,200 ms and the power parameter was "20" in the one electrode discharge, at which time the initial formation of microbubble. Finally, the size of the microbubble was monitored during further discharge and the applied pressure, discharge time and discharge power were continuously adjusted in order to fully expand the gas within the fibers to form microbubble. The fabrication process of FPI_R is shown in Fig. 1(b). Firstly, the SMF with one end face being flat was inserted into a HCT (inner/outer diameter: 190/350 μm) and placed into the fusion splicer. The HCT was fused to the SMF by discharging the end of the HCT with the fusion splicer at a discharge power of + 5 and a discharge time of 600 ms. Then, another SMF with a flat end was inserted into the HCT, and the electric motor of the fusion splicer was used to adjust the distance between the end faces of the fiber in the capillary to acquire the interference spectrum. Subsequently, the end of the HCT was discharged using the fusion splicer (discharge power: +5, discharge time: 600 ms) to fuse the HCT and SMF, at which point the two flat SMFs inserted into the HCT formed an air cavity.

The optical microscopy image of the FPI_S is shown in Fig. 2(a). By adjusting the driving motor, discharge time, and discharge power of the fusion splicer, the axial diameter of the FPI_S bubble is 53.05 μm, the longitudinal diameter of the FPI_S bubble is 66.15 μm, and the minimum wall thickness of the FPI_S is about 3.02 μm. The smaller wall thickness acts on the bubble and makes it sensitive to external environmental changes. The optical microscopy image of FPI_R composed of SMF and HCT is shown in Fig. 2(b). The two SMFs inserted into a HCT form an air cavity with a length of 63.69 μm.

Fig. 3(a) illustrates the sensing principle of FPI_S, where M_1 and M_2 are the two reflective surfaces of the bubble in the fiber optic. The light intensity I_S from the supercontinuum light source enters the optical fiber and reaches M_1 for the first reflection with an intensity of I_1. A part of the light passes through M_1 to reach M_2 for the second reflection with an intensity of I_2. Subsequently, the two reflected light beams are coupled in the core of the SMF to produce interference. Similarly, Fig. 3(b) shows the sensing principle of FPI_R. M_3 and M_4 are the two reflective surfaces, with the first reflection intensity being I_3 and the second reflection intensity being I_4.

Since the quartz/air reflection energy is about 4 %, the intensity of

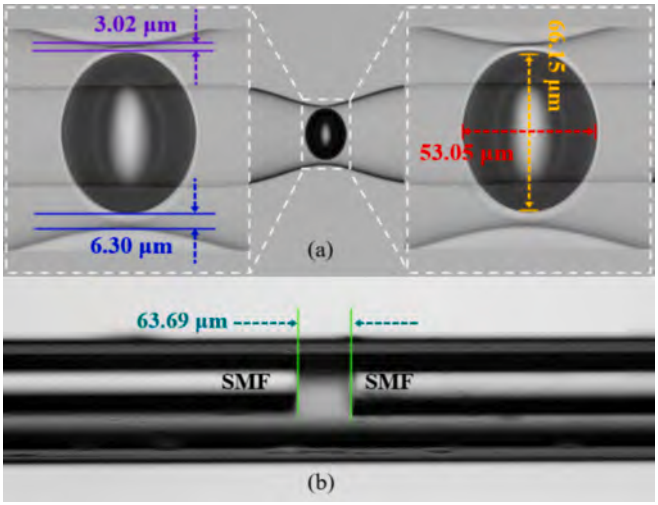

Fig. 2. Micrographs of: (a) FPI_S and (b) FPI_R.

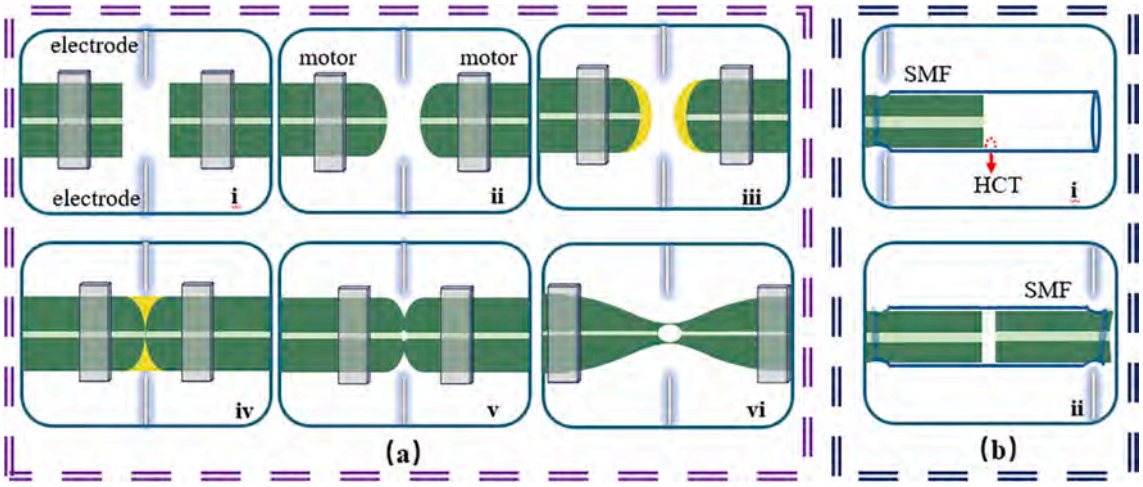

Fig. 1. Schematic illustration of the fabrication of: (a) FPI_S and (b) FPI_R.

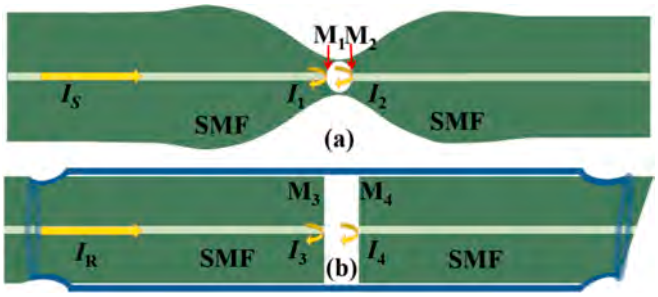

Fig. 3. Sensing principles of: (a) FPI_S and (b) FPI_R.

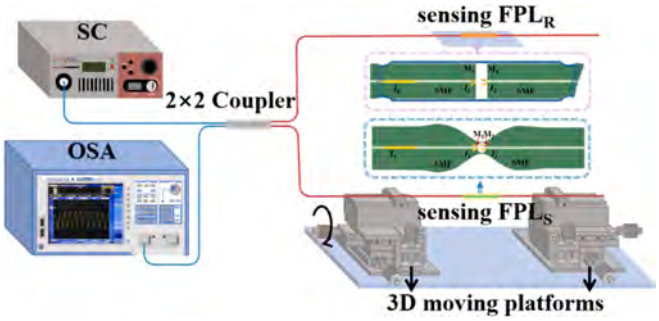

Fig. 4. Schematic diagram of the experimental setup for strain testing.

the third-order reflected light in the FP cavity is only 0.006 % of the original light intensity. The energy of the higher-order reflected light is so weak that it is almost negligible. Therefore, it can be regarded as two-beam interference, namely FPI. For two-beam interference, the expression for the interference spectrum is [25]:

$$I_S = I_1 + I_2 + 2\sqrt{I_1 I_2}COS(\theta)\,, and \tag{1}$$

$$I_R = I_3 + I_4 + 2\sqrt{I_3 I_4}COS(\theta) \tag{2}$$

where $\boldsymbol{\theta}$ is the phase difference shift caused by the transmission of light in the air cavity. With regard to two-beam interference, the reflection spectrum has the cosine characteristic. The Free Spectral Range (FSR) of the reflectance spectrum is expressed by Eq. (3) and Eq. (4) [26]:

$$FSR_S = \lambda_S(m+1) - \lambda_S(m) = \frac{\lambda_S(m+1)\lambda_S(m)}{2n_{eff}L_S} \tag{3}$$

and

$$FSR_R = \lambda_R(m+1) - \lambda_R(m) = \frac{\lambda_R(m+1)\lambda_R(m)}{2n_{eff}L_R} \tag{4}$$

where $\boldsymbol{m}$ is the number of fiber interference levels, $\boldsymbol{\lambda_m}$ is the FPI resonant wavelength position corresponding to the interference level, $\boldsymbol{n_{eff}}$ is the refractive index of air about 1, and $\boldsymbol{L_S}$ is the length of the air bubble and $\boldsymbol{L_R}$ is the length of the air cavity.

In order to further improve the strain sensitivity of the sensor, two parallel FPIs are sued to form the VE. One FPI is the sensing unit, defined as FPI_S, and the other FPI is the reference unit, defined as FPI_R. According to Vernier theory, the envelope $FSR_{envelope}$ can be estimated as:

$$FSR_{envelope} = \frac{FSR_S FSR_R}{|FSR_S - FSR_R|} \tag{5}$$

The magnification factor (M−factor) is an important factor of optical VE. Considering FSR_S as the FSR of the sensing interferometer, the M−factor is expressed as[27,28]:

$$M = \frac{FSR_{envelope}}{FSR_S} = \frac{FSR_R}{FSR_R - FSR_S} \tag{6}$$

The M−factor is also defined as the ratio of the sensitivity of the Vernier envelope to the sensitivity of the sensing interferometer (S_S): [29,30]

$$M = \frac{S_{envelope}}{S_S} \tag{7}$$

3. Experimental setup

Fig. 4 shows a schematic of the experimental setup for strain measurement. 2 × 2 coupler is connected to a Supercontinuum light source (SC, 450–2500 nm) and an Optical Spectrum Analyzer (OSA) at one end, and FPI_S and FPI_R at the other end, respectively. The distance between the two moving platforms is set to 20 cm, and the axial stress applied to the sensor is 200 με at a time. At this point, it is only necessary to place the FPI_S on the two three-dimensional (3D) moving control platforms, while the FPI_R is placed and fixed on the glass slides as a reference.

4. Results and discussion

Fig. 5(a) and (b) show the raw FPI_S and FPI_R spectra in the wavelength range of 1,400 to 1,580 nm, with FSR_S of 20.82 nm and FSR_R of 17.20 nm. The superimposed spectrum after combining FPI_S and FPI_R is shown in Fig. 5 (c). The lower envelope curve of the superposition spectrum is especially obvious, and the measured value of $FSR_{envelope}$ is 99.13 nm, which is in high agreement with the theoretically calculated value of 98.92 nm in Eq. (5). The raw spectra are converted by Fast Fourier Transform (FFT) into spatial frequency spectra, as shown in Fig. 5 (d-f). According to the FFT theory, the spatial frequency response is the inverse of the FSR. As shown in Fig. 5(d) and (e), there is only one dominant frequency component in each, labeled as Peak 1 (f = 0.0480 nm^{-1}) and Peak 2 (f = 0.0581 nm^{-1}). Fig. 5(f) shows the spatial frequency response after connecting FPI_S and FPI_R in parallel. Due to slight detuning in the design, the corresponding FFT peaks (Peak 1 and Peak 2) are close in frequency, and the two adjacent dominant peaks correspond to those in Fig. 5(d) and (e).

Fig. 6(a) and (b) show the forward and reverse strain measurements after applying from 0 to 1,200 με to the single FPI_S. The microbubble inside the optical fiber sensor deforms slightly as the external stress varies, and the wavelength change is proportional to the strain. The forward strain sensitivity of 8.84 pm/με and the reverse strain sensitivity of 8.82 pm/με are calculated from the values of the wave valley near 1,540 nm, and the corresponding linearities are 0.9989 and 0.9991, respectively.

In order to improve the response of the sensor, the FPI_S is connected in parallel with FPI_R to approximate the FSR to form VE. The connection is shown in Fig. 4. Since the FSR of the FPI_R is smaller than that of the FPI_S, as the strain increases from 0 to 1,200 με, the envelopes shift to a smaller wavelength opposite to the shift direction of the single FPI_S, as shown in Fig. 7 (a). The strain variation with stress decreases from 1,200 με to 0 με and demonstrated in Fig. 7 (b). Fig. 7 (c) shows that the forward strain sensitivity is 42.04 pm/με with a linearity of 0.9946, and the reverse strain sensitivity is 41.66 pm/με with a linearity of 0.9896. These two sensitivities are very close to each other confirming the excellent reproducibility and reversibility of the sensor. Moreover, the sensitivity is about 4.76 times that of the single FPI_S sensor, which is in good agreement with the theoretical calculations.

Stability tests on the sensor are performed at room temperature. The interference spectrum is collected for each increment of 200 με with a forward application of 0–1,200 με and held for 5 min. As shown in Fig. 7 (d), the stability is verified by the consistency of the reflectance spectral valley near 1,500 nm under different strains. Additionally, the strain is kept at 200 με, and the reflectance spectra of the sensor are recorded every 10 min for 60 min, as shown in the inset in Fig. 7 (d). The variation of the interference fringes is less than 20 pm, probably because the complex environment of the experimental platform inevitably produces

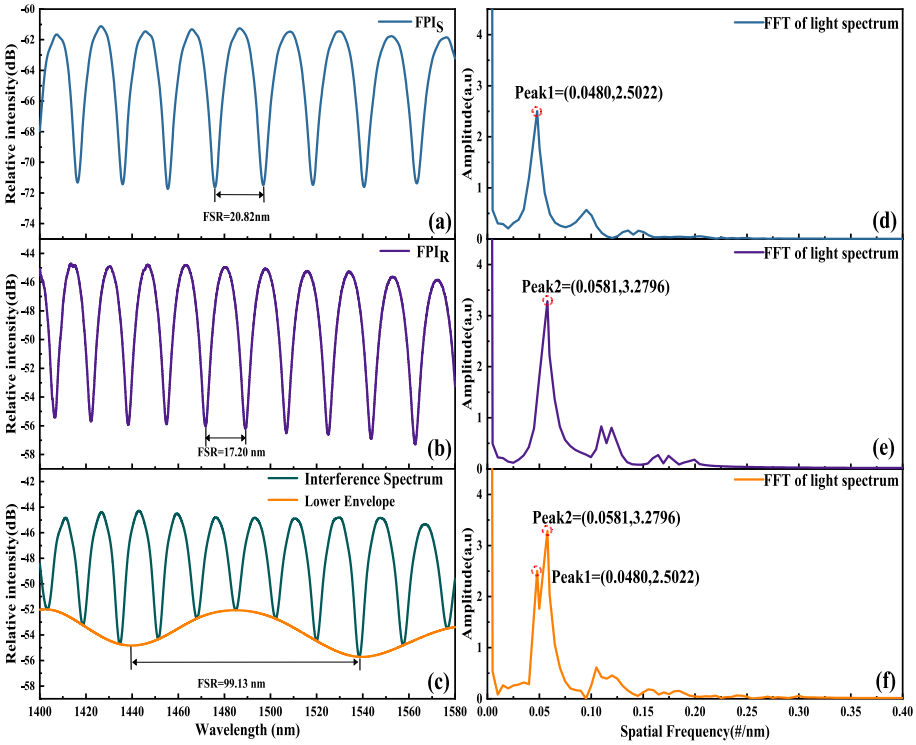

Fig. 5. (a) Interference spectra of FPI_S; (b) Interference spectra of FPI_R; (c) Interference spectrum of the sensor consisting of FPI_S and FPI_R in parallel; (d) Spatial frequency spectra of FPI_S; (e) Spatial frequency spectra of FPI_R; (f) Spatial spectrum of the sensor consisting of FPI_S and FPI_R in parallel.

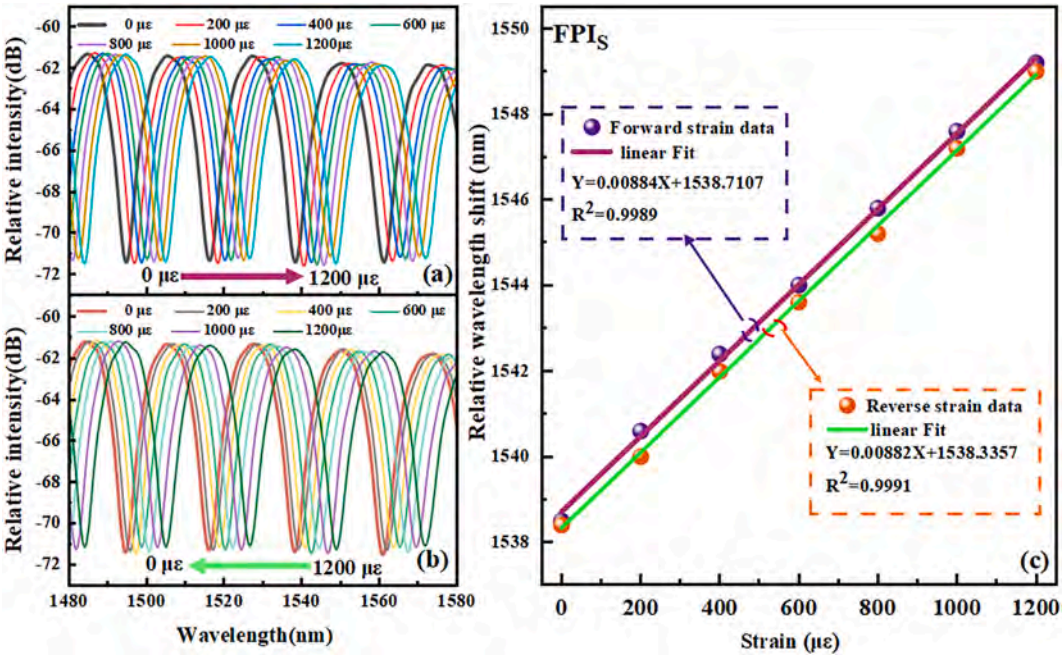

Fig. 6. Strain response of the FPI_S: (a) Forward strain test, (b) Reverse strain test, and (c) Strain sensitivity.

slight vibrations that bias the data and small errors in the stability experiments. All in all, the sensor exhibits good stability.

In the temperature test, the FPI_S fiber is fixed with high-temperature tape on the middle platform of the far-infrared rapid-drying oven, and the FPI_R is in a room-temperature environment. As shown in Fig. 8 (a), the temperature is increased from 30 °C to 150 °C in steps of 20 °C, and the interference spectra are collected after each temperature point is stabilized. Due to the extremely low thermo-optical and thermal expansion coefficients of air and quartz fibers, the interference spectra remain essentially stable during the warming process, as shown in the inset of 8 (a). As shown in Fig. 8 (b), the temperature sensitivity of the sensor is only 0.936 pm/°C, and the calculated temperature cross-sensitivity is 0.022 με/°C. This confirms that the temperature crosstalk is extremely low and can be ignored in practical applications.

The properties of our sensor are compared to those of similar VE-based strain sensors reported recently in terms of working range,

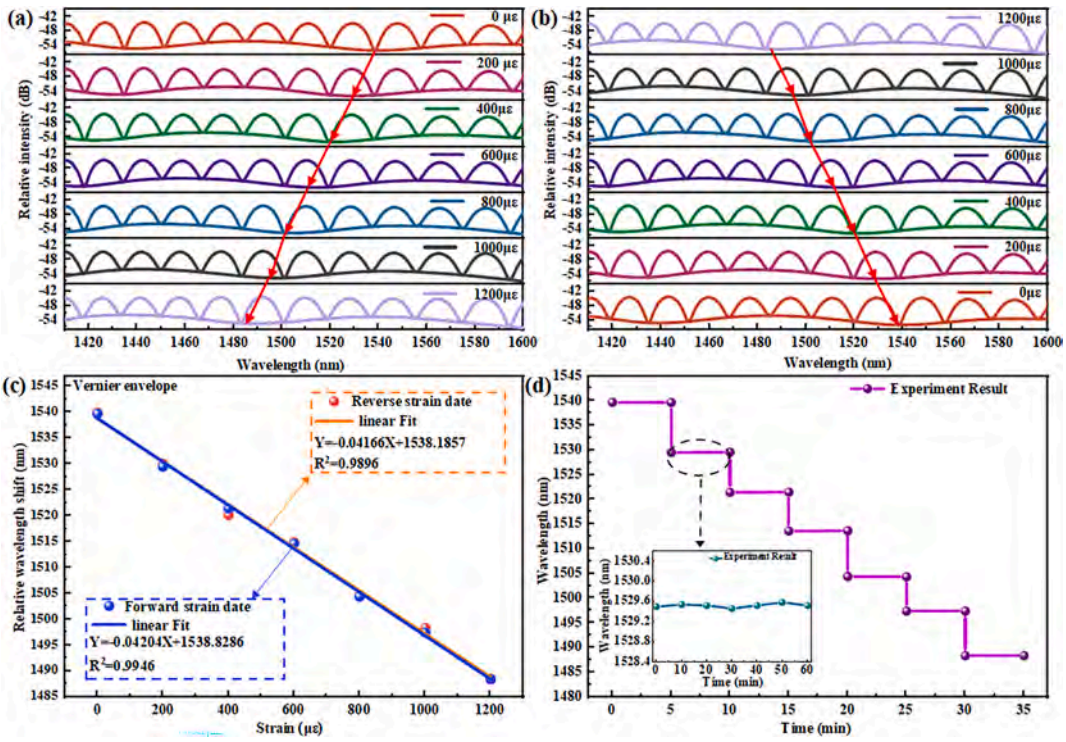

Fig. 7. Strain response and stability of the sensor of FPI_S and FPI_R in parallel: (a) Forward strain test, (b) Reverse strain test, (c) Strain sensitivity, and (d) Stability.

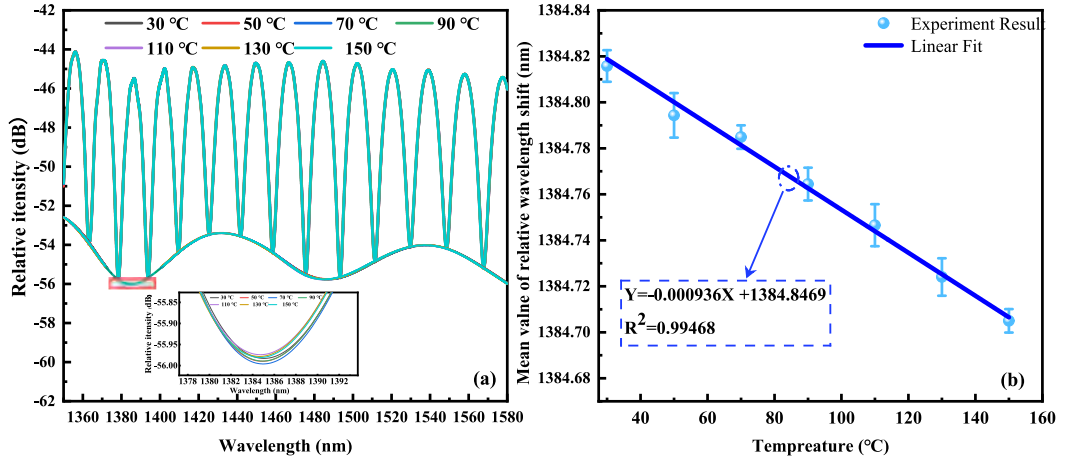

Fig. 8. Temperature response: (a) Reflection spectra of the sensor at different temperatures and (b) Relationship between the mean value of dip wavelength shift and temperature.

strain sensitivity, and temperature sensitivity, as shown in Table 1. Our sensor shows a high strain sensitivity, a small temperature sensitivity, as well as a temperature cross-sensitivity of 0.022 με/°C. Furthermore, the sensor can be manufactured without costly equipment or hazardous chemicals, consequently increasing the safety and cost-effectiveness in mass production.

5. Conclusion

A highly sensitive air microbubble strain sensor based on the Vernier effect is designed and demonstrated to have a strain sensitivity that is 4.76 times better than that of the single FPI sensor. The sensor has the advantages of simple preparation, easy operation, high success rate, and low cost. The experimental results reveal that the parallel-structured sensor has an ultrahigh strain sensitivity of −42.04 pm/με as well as temperature sensitivity and temperature cross-sensitivity of 0.936 pm/°C and 0.022 με/°C, respectively, consequently reducing the measurement errors caused by temperature variations. In addition, the strain sensor is highly repeatable and stable, thus demonstrating great commercial potential.

CRediT authorship contribution statement

Jingwei Lv: Writing – review & editing, Writing – original draft. **Weijie Kong:** Writing – original draft, Conceptualization. **Jianxin Wang:** Validation. **Wei Li:** Validation. **Renfeng Li:** Validation. **Liangliang Li:** Validation. **Qiang Liu:** Validation. **Jianing Shi:** Validation. **Wei Liu:** Validation. **Pan Meng:** Validation. **Xinrui Guo:** Validation. **Paul K. Chu:** Writing – review & editing. **Chao Liu:** Validation.

Table 1
Comparison between our sensor and previously reported FPI-based sensors.

References	Sensor Configuration	Effective Detection Range (με)	Strain Sensitivity (pm/με)	Temperature Sensitivity (pm/℃)
[30]	Two cascaded FPIs	0–444.4 με	37.3 pm/με	0.7 pm/℃
[23]	Two cascaded FPIs	0–1,400 με	28.11 pm/με	278.48 pm/℃
[13]	Two parallel FPIs	0–1,750 με	−43.2 pm/με	−27 pm/℃
[24]	Two parallel FPIs	0–1,000 με	−14.9 pm/με	0 pm/℃
[3]	MZI − FPI parallelI	0–1400 με	−5.95 pm/με	−279.99 pm/℃
[31]	Two parallel FPIs	0–400 με	36.7 pm/με	1 pm/℃
This work	Two parallel FPIs	0–1,200 με	−42.04 pm/με	0.936 pm/℃

Declaration of competing interest

The authors declare that they have no known competing financial interests or personal relationships that could have appeared to influence the work reported in this paper.

Acknowledgments

This work was jointly supported by the National Natural Science Foundation of China [12304480], Heilongjiang Provincial Natural Science Foundation of China [JQ2023F001], Local Universities Reformation and Development Personnel Training Supporting Project from Central Authorities, the Basic Research Support Project for the Excellent Youth Scholars of Heilongjiang Province[YQJH2023077], Study Abroad returnees merit-based Aid Foundation in Heilongjiang Province [070-719900103], and City University of Hong Kong Donation Research Grants [DON-RMG 9229021 and 9220061].

Data availability

Data will be made available on request.

References

[1] L. Deng, C. Jiang, X. Guo, et al., Ultra-sensitive strain sensor composed of tapered two-mode fiber micro-cantilever inserted into quartz capillary, Opt. Fiber Technol. 84 (2024) 103738.
[2] H. Zhang, C. Jiang, X. Zhu, et al., High-sensitivity transverse-load and axial-strain sensor based on air-bubble Fabry–Pérot cavity and fiber Sagnac loop cascaded, IEEE Sens. J. 23 (6) (2023) 5795–5802.
[3] L. Zhao, S. Hao, Y. Chen, et al., Simultaneous measurement of strain and temperature based on fiber sensor with Vernier effect, Opt. Laser Technol. 157 (2023) 108670.
[4] H. Zhang, M. Zhang, J. Kang, et al., High sensitivity fiber-optic strain sensor based on modified microfiber-assisted open-cavity Mach-Zehnder interferometer, J. Lightwave Technol. 39 (13) (2021) 4556–4563.
[5] Y. Hu, H. Wei, Z. Ma, et al., Microbubble-based optical fiber Fabry-Perot sensor for simultaneous high-pressure and high-temperature sensing, Opt. Express 30 (19) (2022) 33639–33651.
[6] R. Min, Z. Liu, L. Pereira, et al., Optical fiber sensing for marine environment and marine structural health monitoring: a review, Opt. Laser Technol. 140 (2021) 107082.
[7] M.F. Bado, J.R.J.S. Casas, A review of recent distributed optical fiber sensors applications for civil engineering structural health monitoring, Sensors (Basel) 21 (5) (2021) 1818.
[8] L. Cai, J. Wang, M. Chen, et al., A high-sensitivity strain sensor based on an unsymmetrical air-microbubble Fabry-Pérot interferometer with an ultrathin wall, Measurement 181 (2021) 109651.
[9] S. Pevec, D.J.O.l. Donlagic, Miniature fiber-optic sensor for simultaneous measurement of pressure and refractive index, Opt. Lett. 39 (21) (2014) 6221–6224.
[10] F. Favero, L. Araujo, G. Bouwmans, et al., Spheroidal Fabry-Perot microcavities in optical fibers for high-sensitivity sensing, Opt. Lett. 20 (7) (2012) 7112–7118.
[11] S. Liu, K. Yang, Y. Wang, et al., High-sensitivity strain sensor based on in-fiber rectangular air bubble, Sci. Rep. 5 (1) (2015) 7624.
[12] Y.-J. Rao, M. Deng, D.-W. Duan, et al., Micro Fabry-Perot interferometers in silica fibers machined by femtosecond laser, Opt. Express 15 (21) (2007) 14123–14128.
[13] T. Nan, B. Liu, Y. Wu, et al., Ultrasensitive strain sensor based on Vernier-effect improved parallel structured fiber-optic Fabry-Perot interferometer, Opt. Express 27 (12) (2019) 17239–17250.
[14] H. Qiu, J. Tian, Y.J.O.E. Yao, Ultrasensitive refractive index fiber sensor based on high-order harmonic Vernier effect and a cascaded FPI, Opt. Express 31 (8) (2023) 13053–13064.
[15] Y. Zhao, X.-X. Wang, R.-Q. Lv, et al., Highly sensitive reflective Fabry–Pérot magnetic field sensor using magnetic fluid based on Vernier effect, IEEE Trans. Instrum. Meas. 70 (2020) 1–8.
[16] Z. Yan, S. Zhu, Y. Zhang, et al., High-temperature and high-pressure fiber microsphere Fabry–Perot sensor based on Vernier effect and FBG, IEEE Sens. J. 23 (9) (2023) 9301–9307.
[17] S. Chen, P. Pan, T. Xie, et al., Sensitivity enhanced fiber optic temperature sensor based on optical carrier microwave photonic interferometry with harmonic Vernier effect, Opt. Laser Technol. 160 (2023) 109029.
[18] X. An, X. Zhao, Q. Peng, et al., Fiber optic strain sensor based on enhanced harmonic Vernier effect, Opt. Fiber Technol. 87 (2024) 103878.
[19] A.D. Gomes, H. Bartelt, O.J.L. Frazão, et al., Optical Vernier effect: recent advances and developments, Laser Photonics Rev. 15 (7) (2021) 2000588.
[20] W. Naku, J. Huang, C.J.I.S.J. Zhu, Optical fiber sensors based on advanced Vernier effect-a review, IEEE Sens. J. (2024).
[21] X. Zhao, Y. Zhang, W. Zhang, et al., Ultrasensitive Fabry–Perot strain sensor based on Vernier effect and tapered FBG-in-hollow silica tube, IEEE Sens. J. 21 (3) (2020) 3035–3041.
[22] Y. Kong, Y. Ruan, H. Ebendorff-Heidepriem, et al., Microstructured optical fibers based hybrid Fabry–Pérot interferometer structure for improved strain sensing by Vernier effect, IEEE Trans. Instrum. Meas. 71 (2022) 1–14.
[23] J. Deng, D. Wang, Ultra-sensitive strain sensor based on femtosecond laser inscribed in-fiber reflection mirrors and Vernier effect, J. Lightwave Technol. 37 (19) (2019) 4935–4939.
[24] H. Zhang, C. Jiang, J. Hu, et al., Temperature-insensitive optical fiber strain sensor fabricated by two parallel connection Fabry–Perot interferometers with air-bubbles, Rev. Sci. Instrum. 94 (4) (2023).
[25] S. Liu, Y. Wang, C. Liao, et al., High-sensitivity strain sensor based on in-fiber improved Fabry–Perot interferometer, Opt. Lett. 39 (7) (2014) 2121–2124.
[26] Q. Li, J. Wang, H. Mu, et al., A Fabry–Pérot interferometer strain sensor composed of a rounded rectangular air cavity with a thin wall for high sensitivity and interference contrast, Opt. Commun. 527 (2023) 128920.
[27] Y. Li, C. Zhao, B. Xu, et al., Optical cascaded Fabry–Perot interferometer hydrogen sensor based on vernier effect, Opt. Commun. 414 (2018) 166–171.
[28] J. Tian, Z. Li, Y. Sun, et al., High-sensitivity fiber-optic strain sensor based on the Vernier effect and separated Fabry–Perot interferometers, J. Lightwave Technol. 37 (21) (2019) 5609–5618.
[29] Y. Zhao, R.-J. Tong, M.-Q. Chen, et al., Relative humidity sensor based on Vernier effect with GQDs-PVA un-fully filled in hollow core fiber, Sens. Actuators, A 285 (2019) 329–337.
[30] L.G. Abbas, Vernier effect-based strain sensor with cascaded Fabry–Pérot interferometers, IEEE Sens. J. 20 (16) (2020) 9196–9201.
[31] G.A. Lashari, F. Mumtaz, S.J.O.F.T. Ahmed, Strain sensing with parallel air-cavity Fabry-Perot interferometers based on Vernier effect, Opt. Fiber Technol. 74 (2022) 103117.